Available online at www.sciencedirect.com
ScienceDirect
Journal of Power Sources 174 (2007) 228–236
JOURNAL OF POWER SOURCES
www.elsevier.com/locate/jpowsour

Protective nitride formation on stainless steel alloys for proton exchange membrane fuel cell bipolar plates

B. Yang [a], M.P. Brady [a,*], H. Wang [b], J.A. Turner [b], K.L. More [a], D.J. Young [c], P.F. Tortorelli [a], E.A. Payzant [a], L.R. Walker [a]

[a] *Oak Ridge National Laboratory, Oak Ridge, TN 37831-6115, USA*
[b] *National Renewable Energy Laboratory, Golden, CO 80401, USA*
[c] *The University of New South Wales, Sydney 2052, Australia*

Received 23 June 2007; received in revised form 19 August 2007; accepted 30 August 2007
Available online 7 September 2007

Abstract

Gas nitridation has shown excellent promise to form dense, electrically conductive and corrosion-resistant Cr-nitride surface layers on Ni–Cr base alloys for use as proton exchange membrane fuel cell (PEMFC) bipolar plates. Due to the high cost of nickel, Fe-base bipolar plate alloys are needed to meet the cost targets for many PEMFC applications. Unfortunately, nitridation of Fe-base stainless steel alloys typically leads to internal Cr-nitride precipitation rather than the desired protective surface nitride layer formation, due to the high permeability of nitrogen in these alloys. This paper reports the finding that it is possible to form a continuous, protective Cr-nitride (CrN and Cr_2N) surface layer through nitridation of Fe-base stainless steel alloys. The key to form a protective Cr-nitride surface layer was found to be the initial formation of oxide during nitridation, which prevented the internal nitridation typically observed for these alloys, and resulted in external Cr-nitride layer formation. The addition of V to the alloy, which resulted in the initial formation of V_2O_3–Cr_2O_3, was found to enhance this effect, by making the initially formed oxide more amenable to subsequent nitridation. The Cr-nitride surface layer formed on model V-modified Fe–27Cr alloys exhibited excellent corrosion resistance and low interfacial contact resistance under simulated PEMFC bipolar plate conditions.

Keywords: Nitrides; Stainless steels; Corrosion; Electrical properties; Oxidation; Nitridation

1. Introduction

Electrochemical devices ranging from sensors to batteries and fuel cells require components with electrically conductive and corrosion-resistant surfaces. Metallic alloys such as stainless steels are of interest as materials of construction for these components because they are readily manufacturable, exhibit good corrosion resistance in a range of environments, and are relatively inexpensive. However, the Cr-base protective oxide surfaces formed on stainless steels tend to yield high values of interfacial contact resistance (ICR), which can significantly degrade electrical performance [1–7]. An important technological example of this issue is the bipolar plate component for proton exchange membrane fuel cells (PEMFCs) [1–4,8–10].

The bipolar plates serve to electrically connect the anode of one cell to the cathode of another in a fuel cell stack to achieve a useful voltage. They also separate and distribute reactant and product streams through flow-field grooves manufactured into the faces of the plates. Developmental bipolar plate materials under investigation include graphite/carbon-based composites [11,12], polymer-based composites with conductive graphite/carbon fillers [13–15], and metallic alloys with/without surface treatments or coatings [5–7,16–24]. Among the bipolar plate candidates, stainless steels such as austenitic type 316 (~Fe–18Cr–10Ni weight percent, wt.% base) and ferritic type 446 (~Fe–27Cr wt.% base) have received a great deal of interest [5–7,17–22] because they are amenable to low-cost/high-volume manufacturing methods such as stamping to form the flow-field grooves, offer relatively high thermal and electrical conductivities, very low gas permeation rates and excellent mechanical properties. However, the high ICR values from the oxides formed on their surface and their borderline

* Corresponding author. Tel.: +1 865 574 5153; fax: +1 865 241 0215.
E-mail address: bradymp@ornl.gov (M.P. Brady).

0378-7753/$ – see front matter © 2007 Elsevier B.V. All rights reserved.
doi:10.1016/j.jpowsour.2007.08.106

corrosion resistance in the aggressive PEMFC environment (60–80 °C, acidic conditions) [5–7] render them unable to meet durability goals for most PEMFC applications. In particular, dissolution of metallic ions such as Fe from stainless steels in the PEMFC bipolar plate environment poisons the sulfonated fluoropolymer membranes, and results in significantly reduced fuel cell performance [20,21].

Transition metal nitrides are promising candidates for protective coatings for PEMFC metallic bipolar plates due to their combination of high electrical conductivity and good corrosion resistance in many acidic environments [8]. However, deposited coatings have thus far not proven sufficiently viable due to their tendency to contain local areas of inadequate surface coverage, i.e. pin-hole defects. Such pin-hole defects result in accelerated local corrosion in the PEMFC environment and metallic ion contamination of the membrane, resulting in unacceptable fuel cell performance [9,20].

In earlier work [25–27], we demonstrated that a protective Cr-nitride surface layer (CrN/Cr_2N) could be formed on a model Ni–50Cr wt.% alloy by thermal (gas) nitridation. The thermally grown Cr-nitride surface yielded low ICR values, excellent corrosion resistance, and stable behavior in single-cell fuel cell testing under both static and drive cycle bipolar plate test conditions [26,28]. Unfortunately, Ni-base alloys are far too expensive for most PEMFC applications, typically 5–10 times greater cost than Fe-base stainless steel alloys. Similarly nitrided stainless steel alloys would be of great interest as bipolar plate materials (as well as for components in other electrochemical devices). However, the high permeability of nitrogen in commercially viable Fe–Cr base stainless steel alloy compositions (<30 wt.% Cr due to σ phase complications) prevents formation of a protective Cr-nitride surface on thermal nitridation, resulting instead in extensive internal nitridation and subsequent poor corrosion resistance [28–37].

Exploratory studies of the effects of nitride-forming alloying additions (Al, Mo, Nb, Si, Ti, V, and Y), temperature, and nitriding gas on the transition from internal to external Cr-nitride formation for Fe–27Cr wt.% base ferritic alloys were pursued in an attempt to form a protective Cr-nitride surface. This paper reports the discovery that surface Cr-nitride layer formation is possible on ferritic Fe–27Cr wt.% base alloys, but only if an oxide scale is first formed on the alloy. Additions of V were uniquely found to enhance this effect. The nitrided V-modified Fe–27Cr base alloys exhibited high electrical conductivity, low ICR values, and excellent corrosion resistance in simulated PEMFC bipolar plate environments, making them promising candidates for use as PEMFC bipolar plates, as well as for components in other electrochemical devices requiring aqueous corrosion resistance and high electrical conductivity.

2. Experimental procedures

This paper presents findings related to the nitridation of V-modified Fe–27Cr (at 2 and 6 wt.% V) compared to a control, binary Fe–27Cr wt.% alloy. The alloys were arc-melted from high-purity elemental metal and drop cast into ingots. The as-cast ingots were cut into disk or rectangular-shaped coupons with dimensions 12–24 mm and ∼1 mm thickness by electrical discharge machining (EDM). The coupon surfaces were then prepared to a 240 grit finish using SiC paper. The polished coupons were suspended in Mo wire cages and nitrided in an Al_2O_3-tube vacuum furnace. The furnace was first evacuated to 1.3×10^{-5} Pa (10^{-7} Torr) vacuum, backfilled with 96%N_2–4%H_2 (vol.%) gas (referred to as N_2–4%H_2 for conciseness) to 101 kPa (1 atm), sealed, and then heated to either 850 or 900 °C over 4 h. Lower nitriding temperatures were not used due to the increased potential for σ phase formation and embrittlement. The samples were held for 24 h at temperature, and then furnace cooled. The N_2–$4H_2$ gas was held static during the nitriding runs to prevent the constant introduction of trace oxygen/water vapor impurities which would accompany a flowing gas. The furnace system used was equipped with a pressure-relief valve to accommodate the pressure increase during heating associated with the expansion of the N_2–$4H_2$ gas with increasing temperature.

Nitrided samples were characterized by X-ray diffraction (XRD) using Cu Kα radiation, Auger electron spectroscopy (AES), field emission gun transmission electron microscopy (TEM) operated at 200 kV, and scanning electron microscopy (SEM) combined with energy dispersive X-ray spectroscopy (EDS). The AES spectra were acquired at 5 keV incident electron energy, with an angle of incidence of 30° from the surface normal. Sputtering was done with 3 keV Ar^+ ions. Tabulated values of atomic sensitivity factors (C = 0.476; N = 0.918; O = 1.101; V = 0.919; Cr = 1.15; Fe = 0.517) were used for depth profile composition calculations, with an estimated accuracy within ±20% of the value obtained. TEM cross-sections were prepared by focused ion beam milling. Selected coupons were also studied for interfacial contact resistance (ICR) and corrosion behavior under simulated PEMFC conditions.

ICR values were obtained using two pieces of conductive carbon paper that were sandwiched between the coupon faces and two copper plates. The total resistance was measured as a function of contact pressure, a key parameter for fuel cell stack applications. Corrections were made for the resistance of the carbon paper/copper plate interfaces ($R_{C/Cu}$) by calibration, and the obtained values were divided by two to obtain ICR values for a single carbon paper/nitride interface. For samples examined after corrosion exposure, in which only one coupon face was exposed to the test environment, the calculated ICR values were not divided by two and thus represent both sets of carbon paper/nitride interfaces. For simplicity these values are referred to as 2× ICR. Further details of the ICR measurement technique are provided in Ref. [5].

Corrosion behavior was evaluated by linear sweeping (0.1 mV s^{-1}) anodic polarization in H_2SO_4 solution of pH 3 at 80 °C, a simplified simulation of the PEMFC bipolar plate environment. A conventional three-electrode system was used, with a platinum counter electrode and a saturated calomel electrode (SCE) as reference. For cathode-side simulation, the electrolyte was constantly purged with air. Static polarization studies were also performed in a simulated highly aggressive PEMFC environment, consisting of 1 M H_2SO_4 + 2 ppm F^-

solution (pH ∼ −0.3) at 70 °C, purged either with H_2 gas to simulate the PEMFC anode environment or air to simulate the PEMFC cathode environment. In these measurements, the samples were stabilized at E_{corr} for 5 min, and then a specific potential was applied and held for 7.5 h and the current–time curve was registered *in situ*. Two potentials were chosen for the tests: +0.14 V versus SHE for the anode conditions, and +0.84 V versus SHE for the cathode conditions (all voltages in this paper are presented relative to the standard hydrogen electrode (SHE) scale unless otherwise noted).

3. Results

3.1. Corrosion behavior

Anodic polarization curves for nitrided Fe–27Cr, Fe–27Cr–2V, and Fe–27Cr–6V in aerated pH 3 sulfuric acid at 80 °C are shown in Fig. 1. Also shown for comparison are data for the model nitrided Ni–50Cr alloy, type 316 stainless steel (a baseline, candidate bipolar plate stainless steel alloy), and untreated Fe–27Cr–6V (metal). The nitrided Fe–27Cr–6V and Fe–27Cr–2V alloys were observed to have open circuit potentials at ∼400 mV (SHE), and low current densities of less than 1 μA cm^{-2} up to ∼900 mV, comparable to those of nitrided Ni–50Cr (Fig. 1a). The corrosion resistance of the nitrided Fe–27Cr–2V and Fe–27Cr–6V was also significantly better than that of type 316 stainless steel (Fig. 1a) and untreated Fe–27Cr–6V metal (Fig. 1b), with an order of magnitude lower current densities up to 0.8–0.9 V versus SHE (PEMFCs typically operate at 0.6–0.8 V, although excursions to 0.9 V and higher are encountered, particularly in automotive applications). In contrast, the open circuit potential of the nitrided binary Fe–27Cr coupon was only ∼150 mV (SHE) and the current densities significantly higher (worse) than the other materials over the 0.6–0.9 V potential range of interest.

Based on the promising dynamic polarization behavior, the 850 °C nitrided Fe–27Cr–6V alloy was selected for further study. Static polarization studies under simulated highly aggressive PEMFC bipolar plate conditions using 1 M sulfuric acid + 2 ppm F^- at 70 °C were pursued to better assess stability in the fuel cell environment (effectively an accelerated corrosion screening protocol) (Fig. 2). Under simulated cathode conditions at +0.84 V and air sparging (Fig. 2a), the current densities reached 3 μA cm^{-2} in 60 min, and gradually stabilized at 1.5–2 μA cm^{-2} at the end of the test. Under simulated anode conditions at +0.14 V and H_2 sparging (Fig. 2b), the current densities decreased to about −9 μA cm^{-2} in 300 min, then gradually stabilized at −6 μA cm^{-2}. The negative sign indicates that the surface was cathodically protected, which mitigates the anodic dissolution of the sample. These low current densities indicate the potential for excellent corrosion resistance of the nitrided Fe–27Cr–6V surface in PEMFC environments.

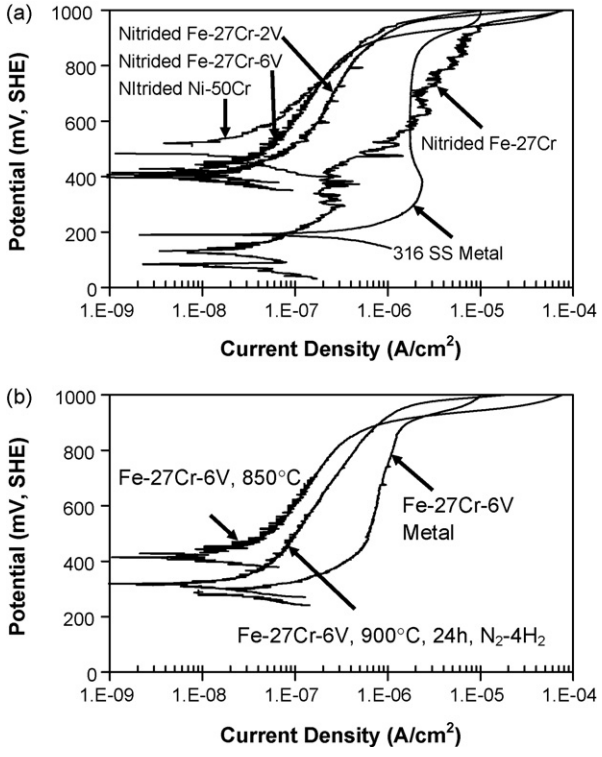

Fig. 1. Anodic polarization curves in aerated pH 3 H_2SO_4 at 80 °C. (a) Fe–27Cr–6V, Fe–27Cr–2V, and Fe–27Cr nitrided in static N_2–$4H_2$ at 850 °C for 24 h, and the Ni–50Cr nitrided in static N_2 at 1100 °C for 2 h, as well as the as-received 316 stainless steel. (b) Fe–27Cr–6V under various treatments of (i) untreated; (ii) nitrided in static N_2–$4H_2$ at 850 °C for 24 h; (iii) nitrided in static N_2–$4H_2$ at 900 °C for 24 h.

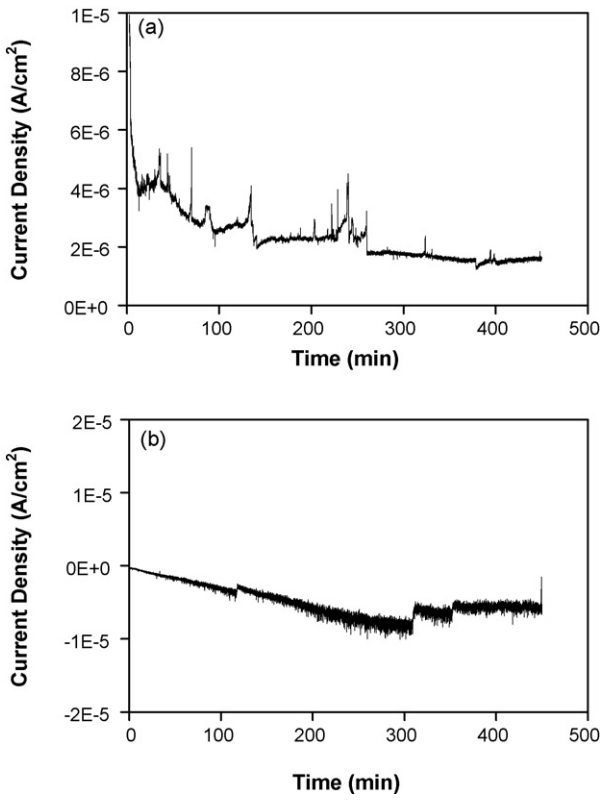

Fig. 2. Static polarization of nitrided Fe–27Cr–6V (850 °C, 24 h, N_2–$4H_2$) for 7.5 h. (a) Held at 0.84 V in 1M H_2SO_4 + 2 ppm F^- at 70 °C with air purge (PEMFC cathode environment). (b) Held at 0.14 V in 1 M H_2SO_4 + 2 ppm F^- at 70 °C with H_2 purge (PEMFC anode environment).

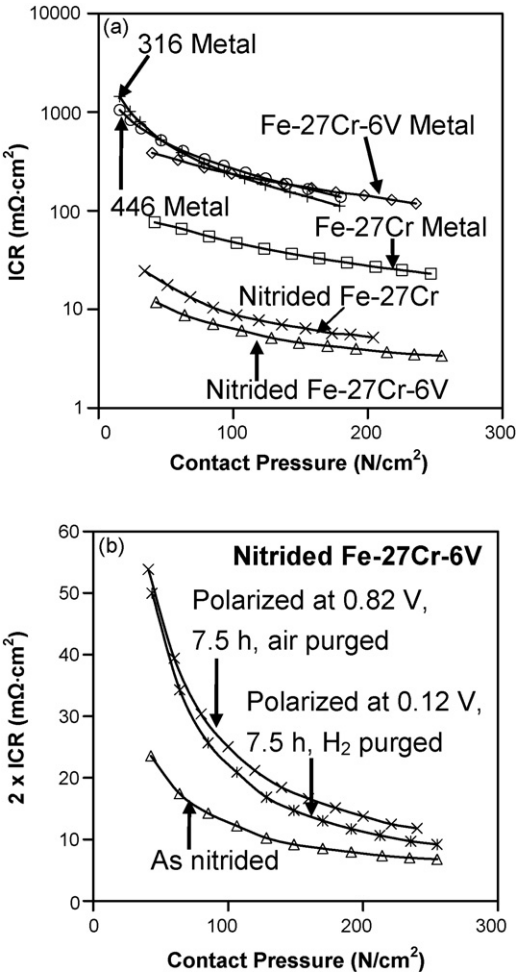

Fig. 3. ICR of stainless steels. (a) ICR of 316 metal, 446 metal, Fe–27Cr–6V metal, Fe–27Cr metal, nitrided Fe–27Cr–6V and Fe–27Cr at 850 °C for 24 h in N_2–$4H_2$. (b) ICR of nitrided Fe–27Cr–6V at 850 °C for 24 h in N_2–$4H_2$ before and after static polarizations in 1 M H_2SO_4 + 2 ppm F^- at 70 °C for 7.5 h.

3.2. ICR measurements

Interfacial contact resistances as a function of contact pressure are summarized in Fig. 3. ICR is a key parameter for fuel cell stacks, where loads are expected to be in the range of only 100–200 N cm^{-2}. Target ICR values at these loads are $<\sim$10 mΩ cm^2, depending on the stack design and application [28]. For all alloys examined, ICR decreased with increased contact pressure. The ICR values for Fe–27Cr–6V metal and type 446 and 316 stainless steels (shown for comparative purposes) were nearly two orders of magnitude higher than the target value. The ICR values for Fe–27Cr metal were an order of magnitude lower, but still well above the target value (Fig. 3a). Subsequent nitridation decreased ICR values by two orders of magnitude for Fe–27Cr–6V, and one order of magnitude for Fe–27Cr (Fig. 3a), to the target range of $<\sim$10 mΩ cm^2 at loads of 100–200 N cm^{-2}. Fig. 3b shows the ICR values for the 850 °C nitrided Fe–27Cr–6V alloy before and after the static 7.5 h polarization holds under simulated highly aggressive anode and cathode conditions (Fig. 2). Polarization in both environments resulted in only a slight increase in the ICR values, but still remained within the target range. In contrast, untreated stainless steel alloys can show high initial ICR values and/or significant increases in ICR values on polarization [5–7].

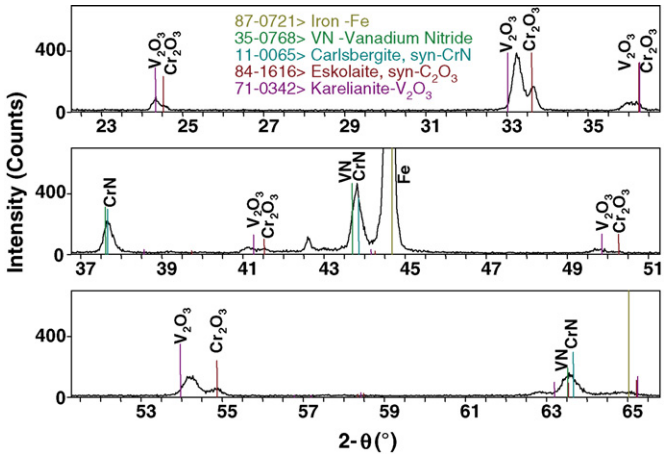

Fig. 4. XRD data for 850 °C nitrided Fe–27Cr–6V. The peaks were consistent with phase mixtures of Cr_2O_3–V_2O_3 and CrN–VN, in accordance with the known phase equilibria, which indicates complete mutual solubility of these oxide and nitride phases, respectively.

3.3. Microstructure characterization

The nitrided Fe–27Cr and Fe–27Cr–6V alloys were chosen for detailed microstructural characterization. Phase identification was based primarily on XRD data, with SEM image microstructural features identified via EDS analysis in light of the XRD results. TEM studies were also performed, and were consistent with the SEM/EDS, XRD, and AES data. A typical XRD pattern is shown in Fig. 4 for 850 °C nitrided Fe–27Cr–6V.

Fig. 5 shows cross-section TEM and SEM micrographs of the surface layer formed on Fe–27Cr nitrided for 24 h at 850 °C in N_2–$4H_2$. It consisted of a single grain thick layer of CrN, approximately 200 nm thick, overlying a continuous underlayer of Cr_2O_3, generally on the order of 0.5–1 μm thick. Regions with poor oxide coverage and little to no nitride surface were also observed (Fig. 5c). Little internal nitridation was evident, consistent with the specific mass change for this alloy on nitridation (0.46 mg cm^{-2}) and the thickness of the surface nitride/oxide layers.

Fig. 6 shows corresponding TEM and SEM micrographs for Fe–27Cr–6V nitrided for 24 h at 850 °C in N_2–$4H_2$. The microstructure consisted of a surface layer of V-doped CrN, (Cr,V)N, with finger-like projections that extended into an inner, mixed region of (Cr,V)N and $(Cr,V)_2O_3$. At the alloy/layer interface, the $(Cr,V)_2O_3$ phase was semi-continuous. The grain size of both phases was on the order of ~200 nm, and the total layer thickness was ~1.5 μm. EDS analysis in the TEM indicated that the V content in the $(Cr,V)_2O_3$ phase varied as a function of depth, with the oxide more V-rich near the alloy/layer interface (approximately 2 V:1 Cr). Fig. 6c shows a low magnification image of the surface layer and the underlying alloy substrate. As with the nitrided Fe–27Cr alloy, essentially no internal nitridation was evident, consistent with the specific mass change for this

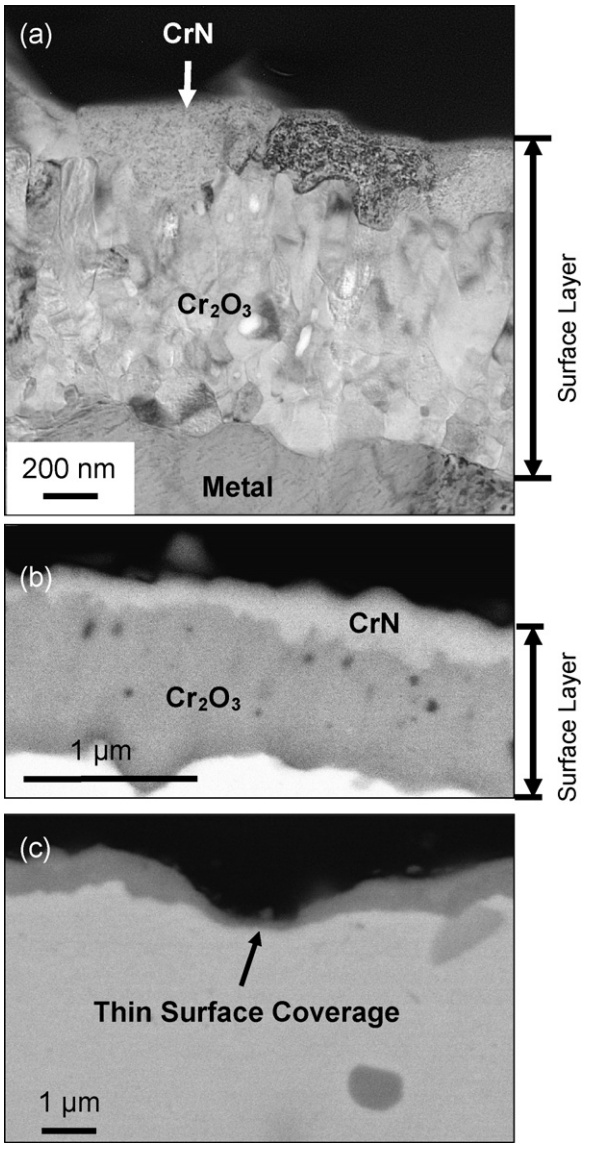

Fig. 5. Microstructure of nitrided Fe–27Cr (850 °C, 24 h, N_2–4H_2). (a) Bright-field cross-section TEM image of the surface scale. (b) Cross-section, backscattered electron SEM image. (c) Occasional gap observed in surface scale region with poor oxide coverage (SEM backscattered electron cross-section image).

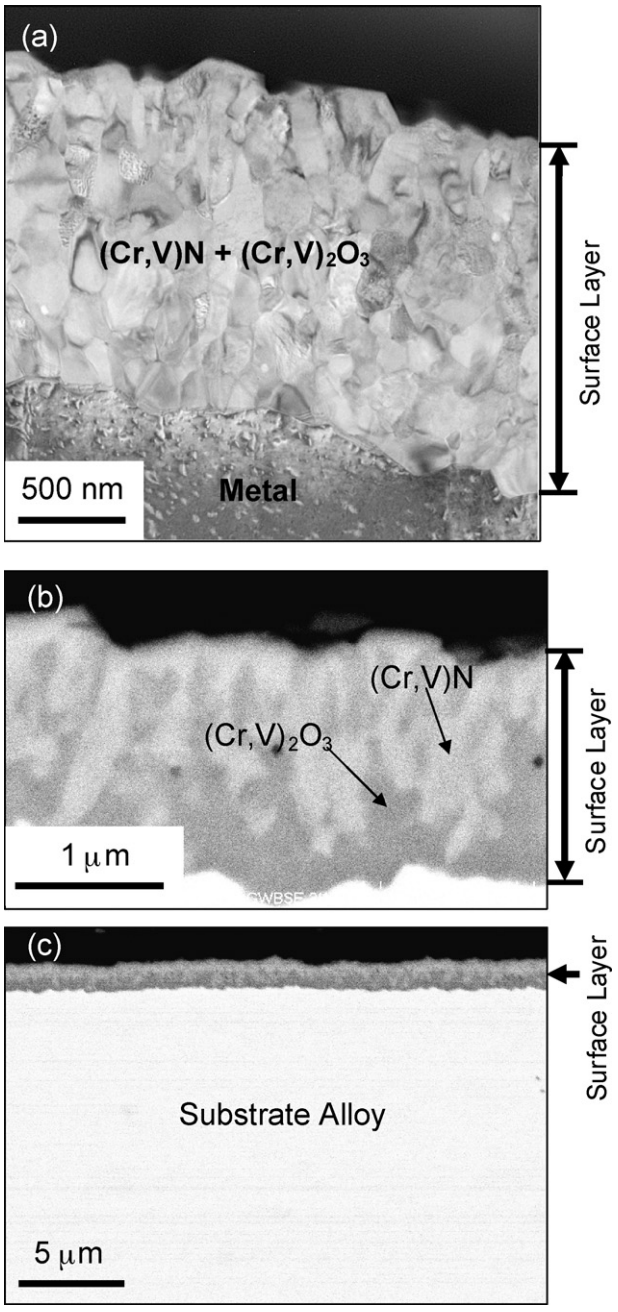

Fig. 6. Microstructures of nitrided Fe–27Cr–6V (850 °C, 24 h, N_2–4H_2). (a) Bright-field cross-section TEM of surface scale. (b) Cross-section SEM image of the scale region (backscattered electron), (c) low magnification cross-section SEM image (backscattered electron).

alloy (0.26 mg cm^{-2}) and the thickness of the nitride/oxide surface layers (internal nitridation for Fe–27Cr alloys under these nitridation conditions results in coarse Cr_2N precipitates readily visible at this low magnification [28]).

Fig. 7 shows corresponding cross-section micrographs for the surface layer formed on Fe–27Cr–6V nitrided for 24 h at 900 °C in N_2–4H_2. The microstructure was similar to that formed on Fe–27Cr–6V at 850 °C (Fig. 6), except that $(Cr,V)_2N$ rather than (Cr,V)N was formed at the surface (based on XRD data). The surface $(Cr,V)_2N$ layer was also thicker than the corresponding (Cr,V)N layer formed at 850 °C, and the grain size coarser. Again, the finger-like projections of the nitride penetrated into an inner region mixed with $(Cr,V)_2O_3$. Internal nitridation was not observed.

To gain further insight into the chemistry of the surface layer formed on 850 °C nitrided Fe–27Cr–6V, AES measurements were performed on samples as-nitrided and after polarization (Figs. 2b, 3 and 8). No Fe was detected in the as-nitrided or polarized sample surface layers. Rather, the surface layers consisted of Cr, N, V, and O species, with enrichment of Cr and N in the outer layer regions and V and O in the inner layer regions, consistent with the SEM and TEM analysis. Three different V signals could be distinguished from the differences in binding energy for the AES data from the as-nitrided sample and were assigned to nitride, oxide, and metal, respectively, as shown in Fig. 8b.

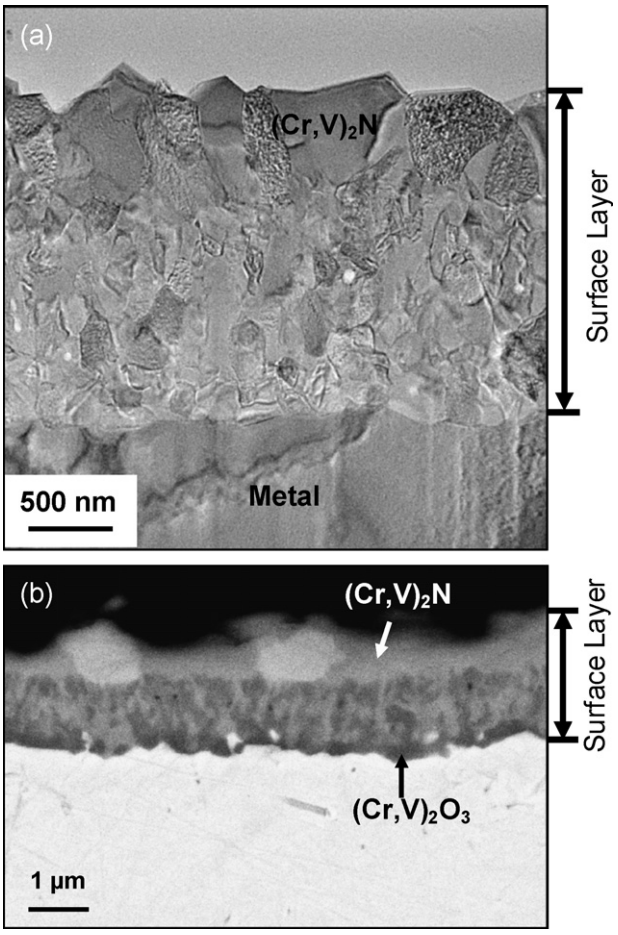

Fig. 7. Microstructure of nitrided Fe–27Cr–6V (900 °C, 24 h, N_2–$4H_2$). (a) Bright-field cross-section TEM image of the surface scale. (b) Cross-section SEM image (backscattered electron).

This analysis suggests that V was present in both the nitride and oxide regions, with the highest relative levels of V located in the respective inner regions of the nitride and oxide layer areas, consistent with its greater thermodynamic stability compared to Cr. The surface chemistries after the static polarizations (Fig. 8c and d) under simulated anodic and cathodic conditions shown in Fig. 2 were very similar to the as-nitrided surface, with the very minor differences, likely, the result of sample to sample variation. This finding is consistent with the excellent corrosion resistance of the nitrided surface (Figs. 1 and 2) and the lack of significant increase in ICR after polarization (Fig. 3b).

4. Discussion

The current densities observed for the nitrided Fe–27Cr–2V and Fe–27Cr–6V alloys in pH 3 sulfuric acid at 80 °C were comparable to those observed for nitrided Ni–50Cr, which has shown good behavior in single-cell fuel cell testing (Fig. 1) [28]. Further, during highly aggressive static polarization holds in 1 M sulfuric acid + 2 ppm F^- under simulated anodic and cathodic conditions, relatively low current densities in the range of 2–6 × 10^{-6} A cm^{-2} were also observed (Fig. 2). Collectively, these data indicate that the nitrided surface layer formed on the V-modified Fe–27Cr alloys offers the potential for a high degree of corrosion resistance under PEMFC conditions.

The nitrided Fe–27Cr–6V alloy also meets the target ICR values. By contrast, untreated type 316 and 446 stainless steels, which have been considered for bipolar plate applications, exhibited ICR values several order of magnitude higher than the target level (Fig. 4a). A key finding was that the low ICR values of the nitrided Fe–27Cr–6V were also retained after static polarization under simulated aggressive anodic and cathodic conditions (Figs. 2 and 4b), with the slight increases observed on polarization still at or below the target 10 mΩ cm^2 value at loads of only 100–200 N cm^{-2}. The combination of corrosion resistance and low ICR values makes these materials of significant interest for PEMFC bipolar plates, as well as for other electrochemical device components requiring a combination of high surface electrical conductivity and corrosion resistance.

The formation of oxides in the surface layer during the nitridation treatment (Figs. 4–8) was a consequence of oxygen impurities in the N_2–$4H_2$ nitriding environment. The oxygen sources included both N_2–$4H_2$ water vapor and oxygen gas impurities, and adsorption of oxygen/water vapor in the furnace when the samples were loaded. Thermodynamically, Cr_2O_3 is much more stable than CrN/Cr_2N.

The effect of oxygen impurities can be calculated from the equilibrium

$$H_2 + (1/2)O_2 = H_2O \quad (1)$$

using standard thermodynamic data. In this way, it was found that at 900 °C, only ~10 ppm of oxygen (present as water vapor) is needed to form Cr_2O_3 in N_2–$4H_2$, as shown in the calculated Cr–N–O stability diagram (Fig. 9). The oxide becomes more favored relative to the nitride with decreasing temperature. It is therefore likely that the oxide was formed during heating to the nitridation temperature. Furthermore, because nitridation in the present work was conducted in a sealed furnace system, oxygen impurities were consumed during the initial reaction stages, with nitride formation subsequently becoming more favored.

Extensive internal nitridation is typically encountered in Fe–Cr base stainless steel alloys during nitriding [28–37]. In the present work, little internal nitridation was observed. This is attributed to the initial formation of the oxide layer during nitriding: Cr_2O_3 for the Fe–27Cr alloy and $(Cr,V)_2O_3$ for the V-modified Fe–27Cr alloys. The presence of oxide on the surface of the alloy is proposed to have retarded the ingress of nitrogen into the alloy, effectively mitigating internal nitridation and permitting external nitride layer formation to occur.

To test the proposed mechanism, nitridation experiments were conducted with flowing N_2–$4H_2$ gas purified with a commercially available molecular sieve cartridge to reduce the level of oxygen and water vapor impurities. Surface and cross-section SEM images of Fe–27Cr–6V nitrided at 900 °C for 4 h using the purified N_2–$4H_2$ gas are shown in Fig. 10. Under these conditions, the alloy was extensively internal-nitrided, with isolated Cr-nitride particles formed on the surface rather than the previously observed continuous Cr-nitride layer (Fig. 10 versus Fig. 7) (some oxide was still formed in the purified gas, but con-

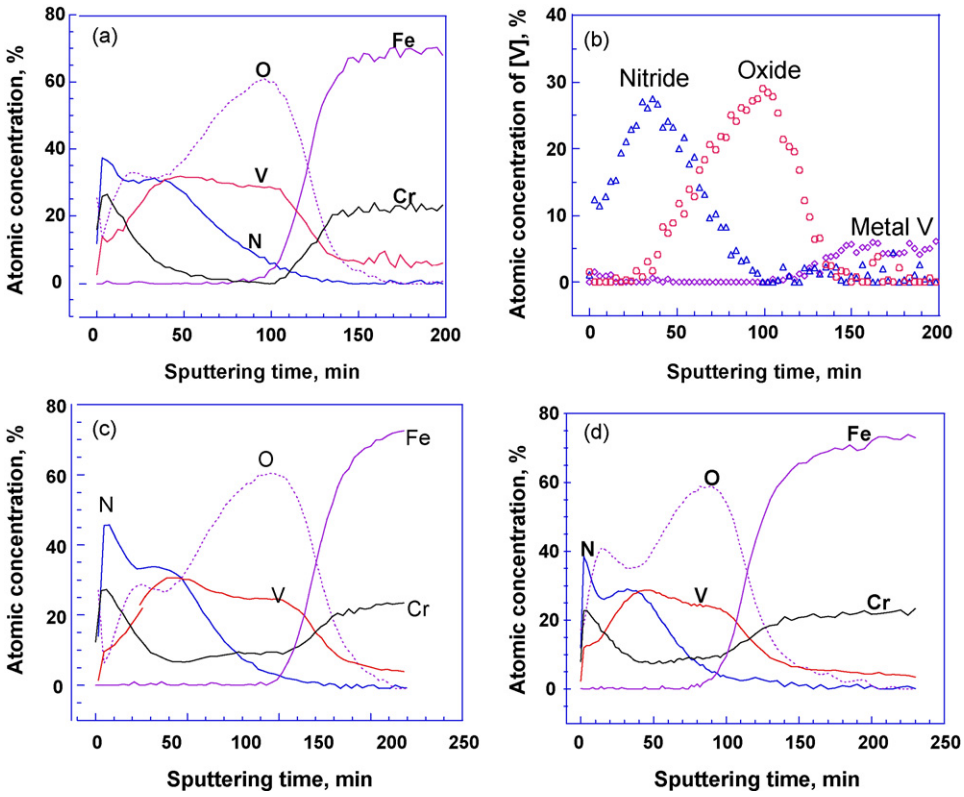

Fig. 8. AES depth profile for nitrided Fe–27Cr–6V alloy (850 °C, 24 h, N_2–$4H_2$). (a) As-nitrided. (b) The vanadium distribution in nitride and oxide of the as-nitrided sample. (c) Polarized at 0.84 V in 1 M H_2SO_4 + 2 ppm F^- at 70 °C with air purged for 7.5 h. (d) Polarized at 0.14 V in 1 M H_2SO_4 + 2 ppm F^- at 70 °C with H_2 purged for 7.5 h. The composition data was calculated based on tabulated sensitivity factors, and is estimated to be within ±20% of the value obtained.

siderably less than the previous conditions). This result therefore supports the hypothesis that initially formed oxide limited internal nitridation, thus permitting external, continuous Cr-nitride layer formation to occur. The initial ease in forming external Cr-oxide on oxidation, relative to internal Cr-nitride formation on nitridation, is attributed to the lower permeability of oxygen in stainless steels than nitrogen.

The corrosion resistance of the CrN/Cr_2O_3 layers formed on Fe–27Cr was relatively poor (Fig. 1). This is attributed to local areas of inadequate surface coverage by the outer CrN layer on Fe–27Cr (Fig. 5). By contrast, the $(Cr,V)_xN$ layer formed on Fe–27Cr–6V at 850 and 900 °C was dense, continuous (Figs. 6 and 7), and yielded corrosion resistance comparable to the model nitrided Ni–50Cr material (Fig. 1). Effectively, there was a greater proportion of nitride to oxide formed on the Fe–27Cr–6V alloy than on the binary Fe–27Cr alloy (Figs. 6 and 7). This greater extent of nitride formation led to the continuous $(Cr,V)_xN$ surface layer and the excellent corrosion resistance of nitrided Fe–27Cr–6V.

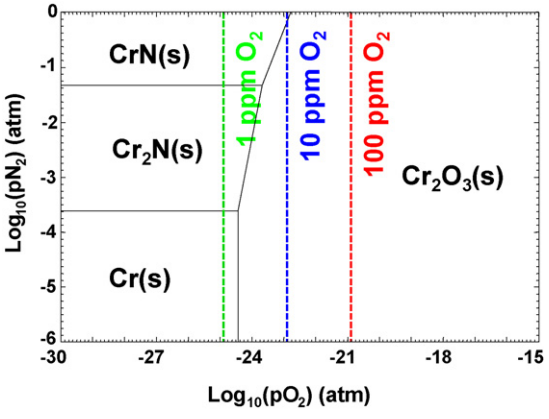

Fig. 9. Calculated Cr–N–O stability diagram for pure Cr exposed at 900 °C in N_2–$4H_2$ with oxygen impurities.

Fig. 11 shows a calculated stability diagram for pure V in N_2–$4H_2$ with oxygen impurities at 900 °C. Compared with the calculation for pure Cr (Fig. 9), VN has greater stability relative to V_2O_3 than does CrN relative to Cr_2O_3, such that the VN is stable to about 100 ppm of oxygen in N_2–$4H_2$, while CrN is stable only to about 10 ppm. Therefore, a Cr–V oxide mixture would be expected to be nitrided in a N_2–$4H_2$ environment containing a higher level of oxygen impurities than would Cr-oxide alone. In other words, V destabilizes the oxide relative to the nitride to a greater degree than does Cr. Thus, the initially formed oxide layer could be more readily converted to nitride (i.e. exhibit the transition to nitride formation at a higher level of oxygen impurities) if it contained V. Vanadium appears to be a unique addition to accomplish these effects in that in addition to the relative thermodynamic oxide/nitride stability properties noted, V_2O_3, V_2N, and VN are all completely soluble in Cr_2O_3, Cr_2N, and CrN, respectively.

The dependence on oxygen impurities in the nitriding environment to initially form oxide to achieve protective Cr-nitride formation resulted in run-to-run variability in the nitrided sur-

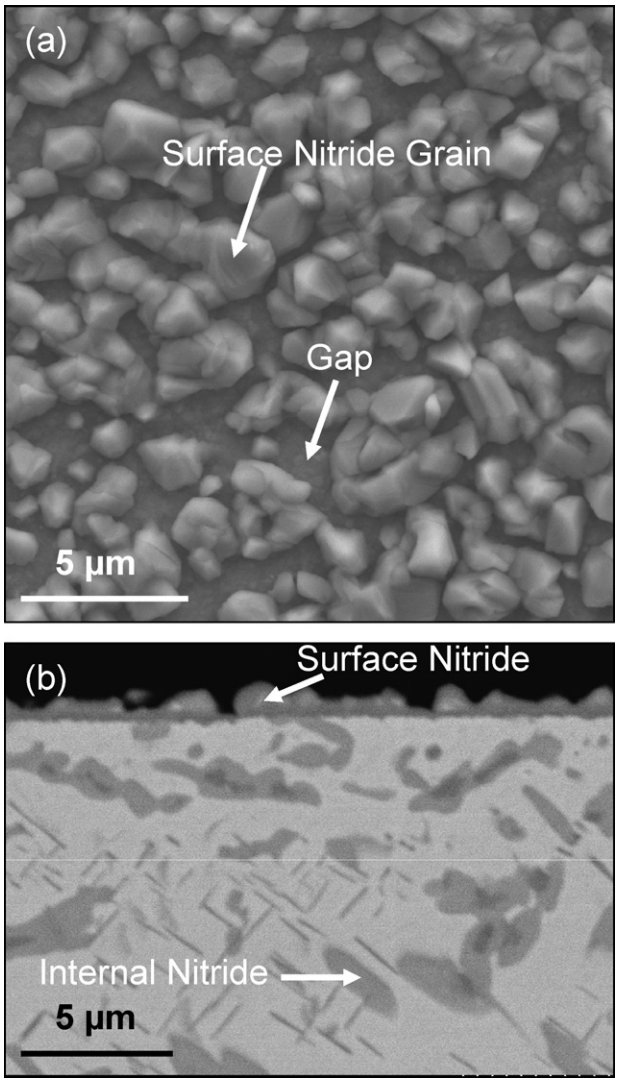

Fig. 10. Microstructure of nitrided Fe–27Cr–6V (900 °C, 4 h, flowing N_2–$4H_2$, with O_2 scrubber). (a) Surface SEM image (secondary electron). (b) Cross-section SEM image (backscattered electron).

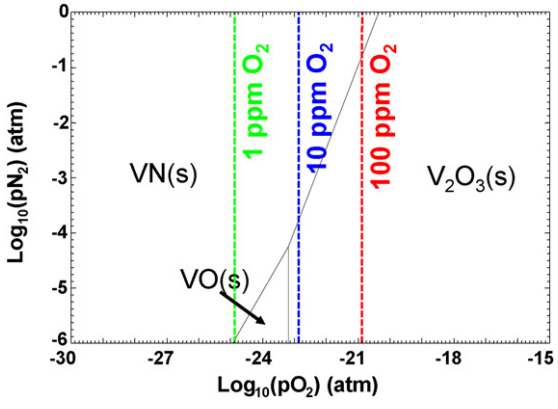

Fig. 11. Calculated V–N–O stability diagram for pure V exposed at 900 °C in N_2–$4H_2$ with oxygen impurities.

face structures that were formed on the V-modified Fe–27Cr alloys. Structures intermediate to the continuous, protective surface layer shown in Fig. 7 and the nonprotective surface shown in Fig. 10 have been observed. This, in turn, has manifested as variations in the degree of corrosion resistance that can be achieved. In order to eliminate this variability, efforts are now focused on preoxidation in flowing gases with controlled levels of oxygen intentionally introduced to consistently form the initial $(Cr,V)_2O_3$ base layer, followed by a nitridation step. Preliminary results for this approach are promising [28]. Best results to date have been obtained via preoxidation at ~900 °C for 30 min to 4 h in flowing Ar–$4H_2$–$0.5O_2$ or N_2–$4H_2$–$0.5O_2$, which yields oxygen uptakes on the order of 0.1–0.2 mg cm^{-2}, followed by nitridation in flowing, oxygen-purified N_2–$4H_2$ at ~900 °C for ~8–24 h (nitrogen uptake on the order of 0.1–0.2 mg cm^{-2}). Higher reaction temperature would be expected to decrease the cycle time needed.

An advantage of this approach is that lower levels of Cr and V in the stainless steel alloy than the model Fe–27Cr–6V alloy of the present work should still be viable, as the oxides of these elements are very thermodynamically stable, and the permeability of oxygen in stainless steels is relatively low. It is estimated that the composition range amenable to this approach can likely be extended downward to 15–20 wt.% Cr and 0.5–3 wt.% V. The lower levels of Cr would be expected to increase alloy ductility and reduce the potential for sigma phase formation, improving alloy manufacturability and suitability for stamping, while reduction in V content will lower alloy cost. It is also likely that the preoxidation/nitridation strategy can be applied to austenitic or duplex stainless steel alloys modified with V, not just ferritic alloys. Austenitic stainless steels generally exhibit higher ductilities than ferritic stainless steels, making them more amenable to manufacturing techniques such as stamping.

5. Conclusions

(1) Protective, electrically conductive (Cr,V)N and $(Cr,V)_2N$ surfaces were formed on Fe–27Cr–6V and Fe–27Cr–2V stainless steels by high-temperature nitridation. The nitrided surfaces demonstrated excellent corrosion resistance and low ICR values in simulated PEMFC environments, establishing them as promising candidate materials for bipolar plates in PEMFCs. These properties also make these materials of interest for other electrochemical devices where a combination of high surface electrical conductivity and aqueous corrosion resistance is needed.

(2) The key to establishing nitride surface layer growth was found to be the initial formation of oxide from oxygen impurities in the nitriding environment. The oxide layer mitigated the high nitrogen permeability of Fe–27Cr, which prevented internal nitridation and permitted external Cr-nitride surface layer formation to occur.

(3) Additions of V were found to enhance the external nitride layer formation on Fe–27Cr alloys. It was postulated that much of the nitride layer formation resulted from conversion of the initially formed oxide. The beneficial effect of V was attributed to the greater relative thermodynamic stabil-

ity of VN to V_2O_3 than CrN/Cr_2N to Cr_2O_3, which resulted in a transition to nitridation at a higher level of oxygen impurities, i.e. V made it easier to destabilize the initially formed oxide to convert it to nitride. Vanadium is uniquely suited to accomplish this because V_2O_3 is completely soluble in Cr_2O_3, V_2N in Cr_2N, and VN in CrN.

(4) The processing approach based on initial oxide formation to block rapid nitrogen permeation of the alloy and enable surface nitride formation during gas nitridation can likely be extended to alloy compositions with lower levels of Cr and V than the model Fe–27Cr–6V studied in the present work. This approach can also potentially be used for the formation of nitride phases other than CrN and Cr_2N, as well as for carbides, borides, etc. phases.

Acknowledgements

This work was funded by the United States Department of Energy (USDOE) Hydrogen, Fuel Cells, and Infrastructure program. Oak Ridge National Laboratory is managed by UT-Battelle, LLC for the USDOE under contract DE-AC05-00OR22725. The authors thank D.F. Wilson, Y. Yamamoto, and Joachim Schneibel for comments on this manuscript, G. Teeter for conducting the AES measurements, and J.M. Vitek and C.E. Duty for input regarding solubility and diffusivity data for the Wagner criteria calculations. The Oak Ridge National Laboratory (ORNL) SHaRE Collaborative Research Center is also gratefully acknowledged.

References

[1] B.C.H. Steele, A. Heinzel, Nature 414 (2001) 345.
[2] S.G. Chalk, P.G. Patil, S.R. Venkateswaran, J. Power Sources 61 (1996) 7.
[3] S.J.C. Cleghorn, X. Ren, T.E. Springer, M.S. Wilson, C. Zawodzinski, T.A. Zawodzinski, S. Gottesfeld, Int. J. Hydrogen 22 (1997) 1137.
[4] V. Mehta, J.S. Cooper, J. Power Sources 114 (2003) 32.
[5] H. Wang, M. Sweikart, J.A. Turner, J. Power Sources 115 (2003) 243.
[6] H. Wang, J.A. Turner, J. Power Sources 128 (2004) 193.
[7] H. Wang, G. Teeter, J.A. Turner, J. Electrochem. Soc. 153 (2005) B99.
[8] R.L. Borup, N.E. Vanderborgh, Mater. Res. Soc. Symp. Proc. 393 (1995) 151.
[9] A. Hermann, T. Chaudhuri, P. Spagnol, Int. J. Hydrogen Energy 30 (2005) 1297.
[10] N.P. Brandon, S. Skinner, B.C.H. Steele, Ann. Rev. Mater. Res. 33 (2003) 183.
[11] T.M. Besmann, J.W. Klett, J.J. Henry, E. Lara-Curzio, J. Electrochem. Soc. 147 (2000) 4083.
[12] J. Scholta, B. Rohland, V. Trapp, U. Focken, J. Power Sources 84 (1999) 231.
[13] D.N. Busick, M.S. Wilson, Proton Conducting Membrane Fuel Cells II, vol. 98-27, The Electrochemical Society, Boston, MA, 1998, pp. 435–445.
[14] J.H. Huang, D.G. Baird, J.E. Mcgrath, J. Power Sources 150 (2005) 110.
[15] N. Cunningham, D. Guay, J.P. Dodelet, Y. Meng, A.R. Hlil, A.S. Hay, J. Electrochem. Soc. 149 (2002) 905.
[16] D.R. Hodgson, B. May, P.L. Adcock, D.P. Davies, J. Power Sources 96 (2001) 233.
[17] R.C. Makkus, A.H.H. Janssen, F.A. de Bruijn, R.K.A.M. Mallant, J. Power Sources 86 (2000) 274.
[18] D.P. Davies, P.L. Adcock, M. Turpin, S.J. Rowen, J. Power Sources 86 (2000) 237.
[19] D.P. Davies, P.L. Adcock, M. Turpin, S.J. Rowen, J. Appl. Electrochem. 30 (2000) 101.
[20] C.L. Ma, S. Warthesen, D.A. Shores, J. New Mater. Electrochem. Syst. 3 (2000) 221.
[21] J. Wind, R. Spah, W. Kaiser, G. Bohm, J. Power Sources 105 (2002) 256.
[22] S. Joseph, J.C. Mcclure, R. Chianelli, P. Pich, P.J. Sebastian, Int. J. Hydrogen Energy 30 (2005) 1339.
[23] N. Aukland, A. Boudina, D.S. Eddy, J.V. Mantese, M.P. Thompson, S.S. Wang, J. Mater. Res. 19 (2004) 1723.
[24] S.J. Lee, C.H. Huang, Y.P. Chen, J. Mater. Process. Technol. 140 (2003) 668.
[25] M.P. Brady, K. Weisbrod, C. Zawodzinski, I. Paulauskas, R.A. Buchanan, L.R. Walker, Electrochem. Solid State Lett. 5 (11) (2002) A245.
[26] M.P. Brady, K. Weisbrod, I. Paulauskas, R.A. Buchanan, K.L. More, H. Wang, M. Wilson, F. Garzon, L.R. Walker, Scripta Mater. 58 (7) (2004) 1017.
[27] I. Paulauskas, M.P. Brady, H.M. Meyer III, R.A. Buchanan, L.R. Walker, Corros. Sci. 48 (10) (2006) 3157.
[28] M.P. Brady, B. Yang, H. Wang, J.A. Turner, K.L. More, M. Wilson, F. Garzon, JOM J. Met. Miner. Mater. Soc. 58 (8) (2006) 50.
[29] K. Tjokro, D.J. Young, Oxid. Met. 44 (1995) 453.
[30] I.C. Chen, D.L. Douglass, Oxid. Met. 34 (1990) 473.
[31] C. Alves Jr., A. de, J. Rodrigues, A.E. Martinelli, Mater. Sci. Eng. A279 (2000) 10.
[32] R.E. Schacherl, P.C.J. Graat, E.J. Mittemeijer, Metall. Mater. Trans. 35A (2004) 3387.
[33] H.J. Grabke, Mater. Corros. (Werkstoffe Und Korrosion) 56 (2005) 384.
[34] T.C. Wang, S. Kimura, Mater. Manuf. Process. 12 (1997) 275.
[35] L.E. Kindlima, G.S. Ansell, Metall. Trans. 1 (1970) 163.
[36] H. Wang, M.P. Brady, K.L. More, H.H. Meyer, J.A. Turner, J. Power Sources 138 (2004) 79.
[37] H. Wang, M.P. Brady, G. Teeter, J.A. Turner, J. Power Sources 138 (2004) 86.